Blue Light for Improved Digital Image Correlation

Schell C, Lester M, LePage W, Keller MW

PUBLISHED AS

Schell C, Lester M, LePage W, Keller MW. "Blue Light for Improved Digital Image Correlation." Experimental Mechanics (2026).

https://doi.org/10.1007/s11340-026-01358-3

Blue Light For Improved Digital Image Correlation

Caroline Schell[1*], Michael Lester[1], William LePage[1], Michael Keller[1]

[1*]Department of Mechanical Engineering, The University of Tulsa, 800 S Tucker Dr, Tulsa, 74104, OK, USA.

*Corresponding author(s). E-mail(s): caroline-schell@utulsa.edu;
Contributing authors: mrl5850@utulsa.edu; lepage@utulsa.edu;
michael-keller@utulsa.edu;

Abstract

Background: Digital image correlation (DIC) of highly curved, complex surfaces often suffers from specular reflection, even when cross polarization is applied. Cross-polarized white light introduces blur and apparent image displacement due to chromatic aberration and wavelength-dependent focal shifts. Objective: This study aims to demonstrate how cross-polarized blue light illumination mitigates optical distortion and improves imaging quality for DIC measurements on curved or reflective surfaces. Methods: A comparative evaluation was performed between traditional cross-polarized white light and cross-polarized blue light during room-temperature tensile tests of specimens with standard acrylic painted speckle patterns. The image quality was compared using grey value counts and confidence parameters from the correlation software. The cross-polarized blue light approach was applied to a complex rubber lattice that was submerged in mineral oil to demonstrate the improvements in image quality for stereo DIC. Results: Blue light illumination produced better speckle contrast, reduced blooming around speckles, and minimized apparent displacement errors compared to white light. Quantitative improvements were observed in the correlation quality metrics. Under cross-polarized white light, the oil-bathed lattice surface was unable to be rendered using commercial DIC software but was fully rendered using cross-polarized blue light. Conclusions: Cross-polarized blue light improves DIC imaging performance on curved, complex, reflective materials by reducing chromatic aberrations and specular glare; a simple modification with monochromatic light for conventional DIC.

Keywords: Digital Image Correlation, DIC, blue light, optical imaging, strain mapping

1 Introduction

Accurate measurement of surface deformation is essential in many engineering and scientific applications. Digital Image Correlation (DIC) is a non-contact technique to measure the deformation of a surface [1]. Measurements via DIC track an applied speckle pattern through sequential images which enables the extraction of full-field displacement data [2].

While DIC excels in standard mechanical tests with simple geometries, such as uniaxial tension or compression, its application to complex surfaces is challenging [3]. Applications to curved geometries, irregular surfaces, and non-traditional loading scenarios such as facial expression analysis [4] or insect wing dynamics [5] can suffer from poor speckle visibility due to specular reflections and uneven illumination levels. Researchers have used many approaches to create high-contrast, trackable speckle patterns under challenging conditions. Solutions include optimized pattern colorways [6], cross-polarized lighting systems [7], fluorescent speckle materials [8], and specific illumination approaches for extreme environments like the use of ultraviolet light for high temperature mechanical testing [9].

Cross-polarization techniques have emerged as a robust approach to improve speckle contrast by reducing surface glare [7, 10]. This method exploits the optical properties of reflected light, which can be decomposed into specular and diffuse components. Specular reflections from flat surfaces have the same polarization orientation of the incident light, while diffuse reflections occur when light penetrates the surface and reemerges in random directions and polarization. By orienting the light source with a linear polarizing filter and placing a perpendicular polarizing filter at the camera, the specular reflection component can be significantly reduced while preserving the diffuse reflection that carries speckle pattern information. While this technique requires brighter illumination due to transmission losses, pattern contrast is improved on smooth, flat, surfaces.

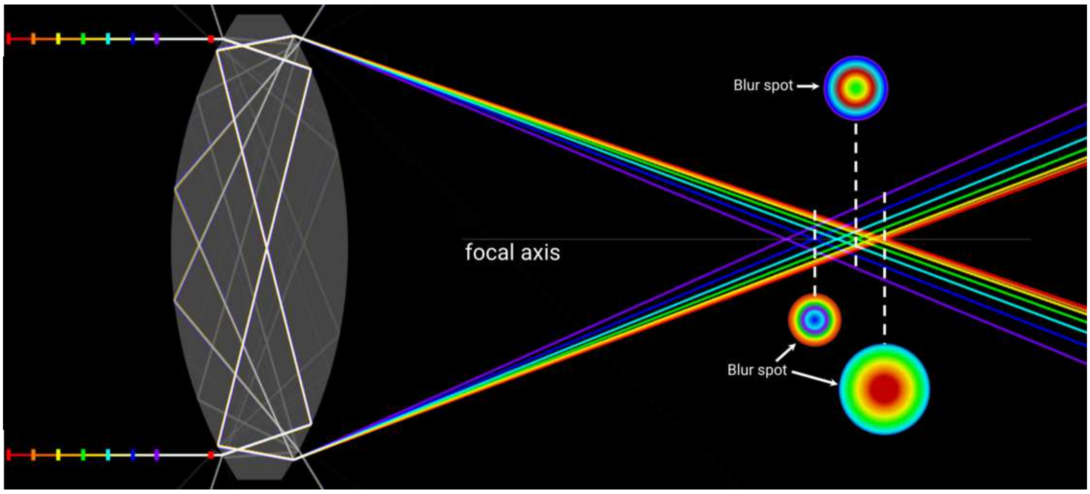

Fig. 1: Blur spot from chromatic aberration at various points along the focal axis. Blue light reduces the minimum spot size and blur by removing the multiple focal points from other wavelengths.

The limitations of cross-polarized stereo (3D) DIC become apparent when applied to curved or complex geometries. On flat specimens, the nearly constant surface normal makes specular reflection geometry more predictable, and cross-polarization can suppress glare because the specular component largely preserves the incident polarization. On curved or complex surfaces, however, the surface normal and plane of incidence vary across the field of view, producing specular highlights at different viewing angles and with varying polarization states; consequently, a single polarizer/analyzer orientation may reduce but not eliminate glare [11, 12].

DIC for complex curved surfaces has been documented in applications ranging from biological specimens, where specular spots on rotator cuff tissue prevented successful correlation [12], to three-dimensional curved surfaces where glare suppression remains challenging despite polarization techniques [11]. Cross-polarization has shown success in some curved applications like bulge testing [13] and 3D imaging of a coin [10], however these examples involve simple curvatures or geometry that minimizes the multi-surface-normal reflection problem.

No current approach to DIC of complex curved surfaces has solved all of the common experimental challenges. The simplest approach—applying matte surface finishes—can reduce specular reflections but is unsuitable for biological samples, subsurface measurements on internal planes, or applications in which surface modification might affect mechanical behavior during large deformation tests [12, 14]. Fluorescent 3D DIC offers a solution that can effectively mitigate specular reflection problems [8, 15]. This technique uses fluorescent particles that emit light when excited by specific wavelengths, with cameras filtered to detect only the fluorescent emission rather than the excitation wavelengths. While effective at fully reconstructing curved surfaces by eliminating reflection-based imaging in lieu of emission-based imaging, this approach requires custom speckle materials that are time-sensitive due to photobleaching [16, 17] and may also be unsuitable for high-temperature applications common in manufacturing processes [18].

The approach described in this paper maintains the well-established acrylic paint speckle patterns that are standard in DIC while mitigating specular reflections on curved surfaces. Here, we combine cross-polarization with monochrome blue light instead of traditional white light. Blue light illumination can eliminate issues like optical bloom or chromatic aberration as well as improving diffuse reflection via Rayleigh scattering [19, 20]. The chromatic aberration and subsequent blur from white, or polychrome light can be seen in Figure 1. While blue light has been used as an illumination source for DIC in high-temperature applications [9, 21, 22], the combination with cross-polarized light has yet to be investigated for use in traditional applications at room temperature. This paper compares the effect of cross-polarized white and blue light in 2D and 3D DIC imaging systems across different strain scales with flat, planar tensile dogbone specimens of both linear-elastic and nonlinear-elastic materials. We then demonstrate the capability to image curved, complex surfaces by applying our method to a reflective, oil-bathed elastomer lattice.

2 Experimental Methods

Cross-polarized white light and blue light DIC testing was conducted on both small strain linear-elastic metals and large strain non-linear elastic materials in uniaxial tensile tests. Due to scaling differences, the DIC set-up and speckle technique were adapted to each application. All representative images shown in this work from 3D DIC tests are taken from the left camera.

Small strain tests were conducted on linear-elastic metallic specimens (NiTi and Ti64) using 2D DIC. These materials served as a control set due to their flat geometries and minimal out-of-plane deformation, providing a baseline for evaluating lighting effects under well-behaved mechanical conditions. The linear elastic behavior of both metals allowed fixed strain levels to be applied without surface conditions changing due to viscoelastic effects.

Large strains were captured using 3D (stereo) DIC on silicone rubber specimens fabricated from a commercial silicone rubber, Dragon Skin 10, that has a reported elongation at break of 1000% by the manufacturer [23]. For this material, we compare our DIC methods at 0% and 50% strain. Since elastomers are capable of reaching large strains, DIC setups must be adjusted to view the entire sample throughout testing, requiring a large depth of focus. The depth of focus can be controlled by closing the aperture [2].

The f-stop number is the ratio of the focal length to the aperture diameter for a lens; closing the aperture increases the depth of focus but decreases light-gathering and increases lens distortion. Consequently, maintaining even brightness and a high contrast speckle pattern across the FOV can be difficult due to reduced the light and increased distortion.

2.1 Materials

2.1.1 NiTi & Ti64

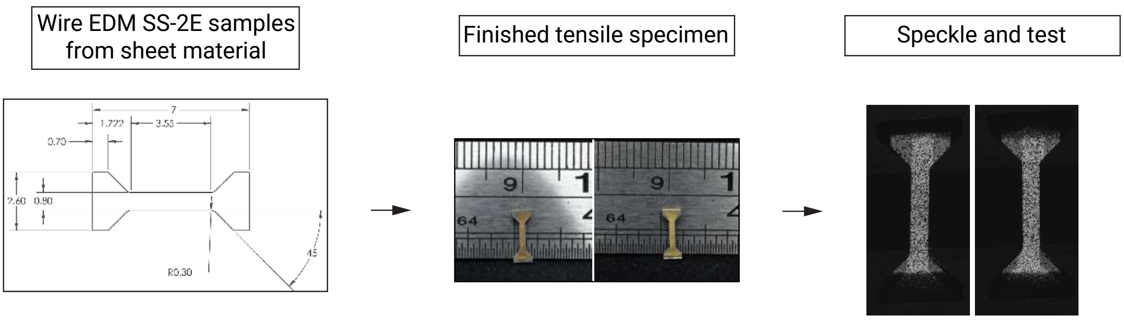

Fig. 2: SS-2E dogbone specimen gemoetry and fabrication method with applied acrylic speckle patterns on Ti64 and NiTi samples.

Speckle patterns were applied with an Iwata Custom Micron CM-B airbrush. A white acrylic base coat was applied first at a pressure of 40 psi, then a black acrylic paint at 80 psi to deposit a speckle pattern on top of the white base. When applying the black speckles, the flow was choked by minimizing the needle travel, which along with the higher operating pressure yielded a speckle size suitable for the small (0.8mm) gauge width.

2.1.2 Silicone rubber

The silicone rubber specimens were fabricated from a laser-cut open faced mold with ASTM D412 standard die A dimensions with a uniform thickness of 2 mm, as seen in Figure 3. Two color schemes were evaluated: a white base with black speckles and a black base with white speckles.

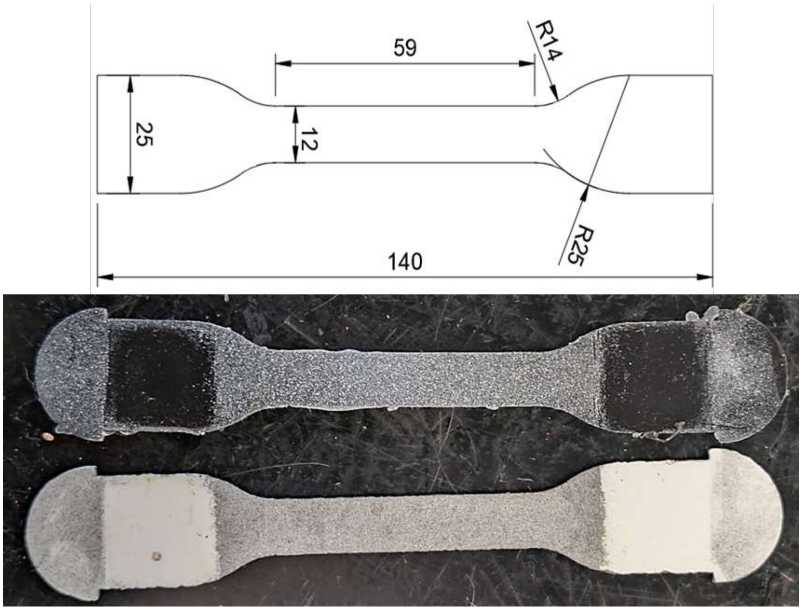

Fig. 3: Dragon Skin 10 specimen dimensions (in mm) used in this study.

Hyperelastic materials can have large deformations out-of-plane and as such require 3D DIC for characterization. Polydimethylsiloxane (PDMS), or silicone rubber, is chemically inert and does not bond to many materials, aside from other silicone rubbers, without surface treatments [24, 25]. This property makes it challenging to apply speckle patterns using the well established methods developed for materials like metals, as acrylic paint layers tend to crack and delaminate from the surface when the rubber is strained. To address this problem in this study, the background of the speckle pattern is the PDMS base itself, such that the only paint applied to the specimen is the speckle.

The specimens were prepared according to manufacturer instructions: Part A is mixed with the Silc-Pig pigment up to 3%, for maximum opacity. After curing in the mold, a strip of clear tape was applied over the gauge section to remove any dust or debris. An Iwata Eclipse Series Airbrush - HP-CS was used to apply black paint for the white base and white paint for the black base at an air pressure of 8-10psi. In Figure 4, speckles were analyzed in ImageJ and found to have an average diameter of 10 microns. This speckle measurement translates to an average diameter of 3 ± 1.4 pixels wide in the uniaxial tensile tests which has the largest FOV of all camera rig combinations. Smaller speckles were found to reduce or eliminate speckle spallation, even at high deformations. Additionally, smaller patterns can be preserved over multiple tests without significant degradation.

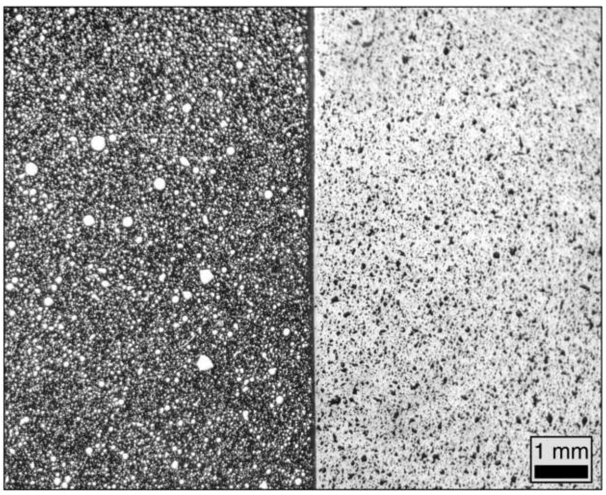

Fig. 4: Acrylic speckle pattern for the Dragon Skin 10 specimen.

2.2 Mechanical Testing Procedures

To evaluate measurement accuracy, rigid body translation tests were conducted on both the dedicated 2D DIC system and a combined 3D + 2D setup, in which the 3D rig was equipped with an additional 2D camera. The rigid body translation tests serve as a baseline reference for the performance of the imaging systems with known displacements.

2.2.1 Rigid Body Translation and Uniaxial Tension: 2D DIC on metals

Rigid body translation (RBT) and low strain tests for the 2D-DIC dogbones were performed on a Psylotech µTS 1.6 kN load frame, with shoulder grips designed for the SS-2E sample geometry. Rigid body translation images were taken in intervals of 1 mm across the field of view of the 2D-DIC camera by moving a secondary stage to which the µTS was attached. A 1 N preload was applied to prevent any movement of the sample in the grips for RBT tests. Ti64 and NiTi samples were pulled in uniaxial tension to engineering strain values between 0 and 0.41% to gather more data points in low strain regimes that were not captured in PDMS samples. The Psylotech load frame was set to force control for those uniaxial tension tests, and three load levels were applied to each sample such that the material stayed in the linear elastic region, ensuring that no plastic deformation remained upon unloading. Images were captured in the Vic-Snap 9 image acquisition software.

2.2.2 Rigid Body Translation: 2D and 3D DIC on silicone rubber

Specimen were excised from dogbone speckled materials described in Section 2.1.2 and glued to a small acrylic plate using Sil-Poxy (Smooth-On, Inc) and superglue. The actuator was moved to displacements of 1, 2, 3, and 4 mm, then returned to 0 mm.

2.2.3 Uniaxial Tension: Large Strain 3D DIC on silicone rubber

A custom load-frame equipped with a 50 N load cell from Interface, Inc. was used in this study. A LabView program controls the crosshead displacement and records load data. A single chassis NI DAQ connects the LabView program to a second computer which simultaneously runs the Vic-Snap 9 program. With this set-up, we can capture the load data at the same acquisition interval set in the Vic-Snap software (500 ms). Pneumatic grips supply a constant pressure on the material to avoid unnecessary strains produced by clamp or wedge grips. The specimens were pulled at a strain rate of 1 mm/s.

2.3 Lighting & Optics

The optical camera parameters and acquisition settings for the uniaxial tensile tests are detailed in Table 1 for the metal specimens and in Table 2 for the silicone rubber specimens. The stereo camera rig was placed sufficiently far away from the sample in order to capture large strains to ensure that the material stays within the camera FOV.

Figure 5 summarizes all imaging configurations used in this study. For the small-scale test rig (top row of Figure 5), a single camera equipped with a telecentric lens served both of the experimental testing procedures detailed in Section 2.2.1 with only the light source swapped between illumination regimes; the camera arrangement remained otherwise unchanged. For the large-scale test rig (bottom row of Figure 5), two distinct configurations were required for the RBT (described in Section 2.2.2) and uniaxial tensile testing (described in Section 2.2.3). The RBT testing required a closer imaging distance dictated by the working distance of the telecentric lens used for the simultaneous capture of 2D DIC images with the two additional stereo cameras capturing 3D DIC images (Figure 5c.) Uniaxial tensile tests of the silicone rubber specimens used only the stereo camera pair for 3D DIC at a larger working distance, as the large deformations required a wider FOV (Figure 5d). In both large-scale setups, white and blue light sources were interchanged for the comparison in this study.

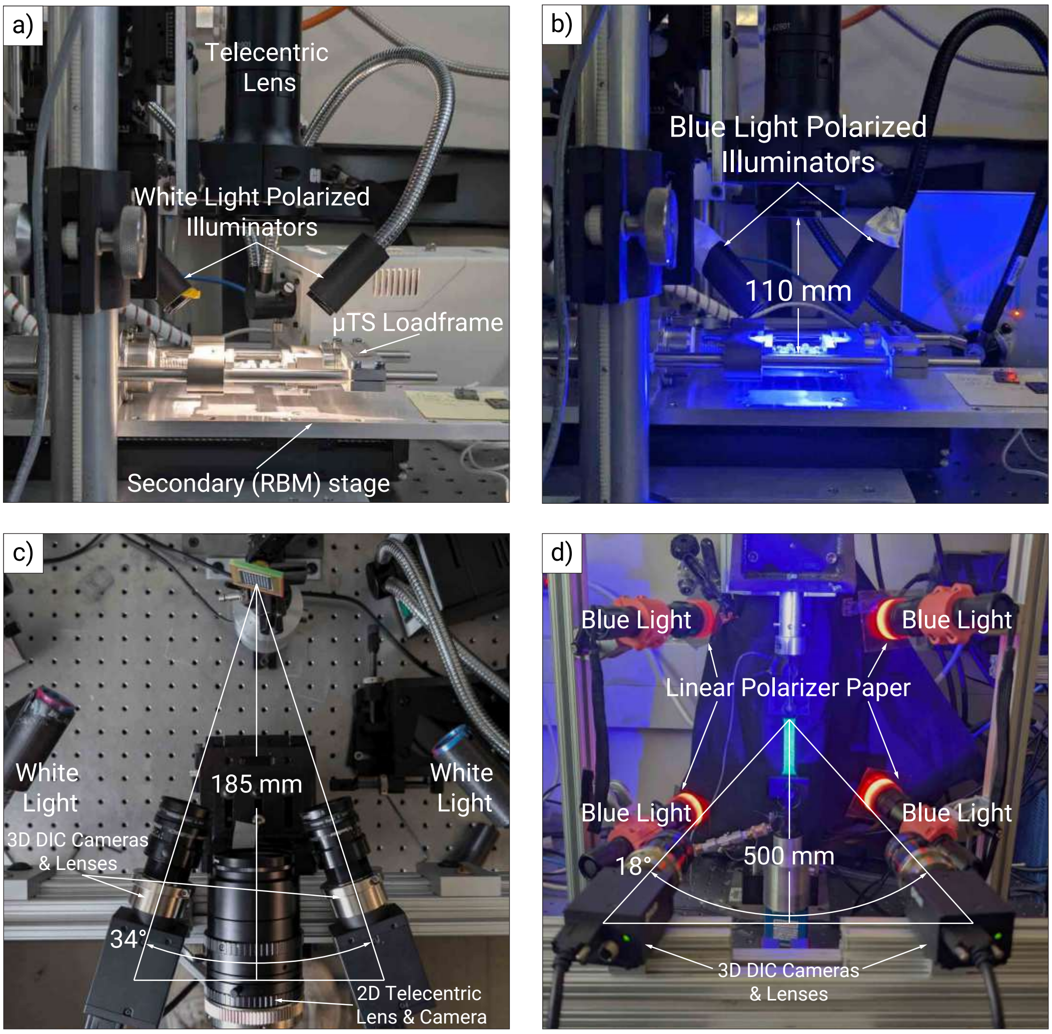

Fig. 5: (a) Small-scale 2D DIC setup under white light illumination, with a single camera equipped with a telecentric lens for imaging of RBT and tensile tests (metals). (b) Same small-scale setup as (a) but under blue light to illustrate illumination swap. (c) Large setup for RBT under white light illumination, with two stereo cameras for 3D DIC and one camera for simultaneous 2D DIC, as labeled. Blue light was substituted for white light in this setup for RBT. (d) Large scale setup for uniaxial tensile testing of silicone rubber specimens under blue light illumination, utilizing only two stereo cameras for 3D DIC; the larger working distance accommodates the wide FOV required to capture the large deformations. White light was substituted for blue light to compare the lighting regimes.

	Rigid Body Translation & Uniaxial Tension	
	White Light	Blue Light
Camera	FLIR Grasshopper3 GS3-U3-123S6M	
Lens	0.9X CobaltTL Telecentric Lens	
Lighting	One dual goose neck halogen lamp	SugarCUBE™ (Digital Light Innovations, 458 nm)
Lens Filter	Linear Polarizer (Mid-Opt PR032)	Linear Polarizer (Mid-Opt PR032) BP470 (Mid-Opt)

Table 1: Equipment list and camera information for the 2D small strain rig used in this study for metal specimen.

	Rigid Body Translation		Uniaxial Tension	
	White Light	Blue Light	White Light	Blue Light
Lighting	One dual goose neck halogen lamp	SugarCUBE™ (Ushio)	Two dual goose neck halogen lamps	Four UltraFire Blue LED lights
Cameras	Three FLIR Grasshopper3 GS3-U3-123S6M		Two FLIR Grasshopper3 GS3-U3-123S6M	
Lenses	Schneider Xenon-Topaz 38mm (3D) Computar TTEC-M55MPW (2D)		Schneider Xenon-Topaz 38mm	
Lens Filters	Heliopan Linear Polarizer (3D) Linear Polarizer (2D)	Heliopan Linear Polarizer (3D) LP395 (Mid-Opt) (3D) Linear Polarizer (2D) BP470 (Mid-Opt)(2D)	Heliopan Linear Polarizer	Heliopan Linear Polarizer LP395 (Mid-Opt)
Aperature	f/8 (3D)	f/8 (3D)	f/4	f/4
Exposure (ms)	10.9	20.0	4.1	7.5
Calibration Grid	9x9 1.78 mm spacing		12x9 6 mm spacing	

Table 2: Equipment list and camera information for the various rigs used in this study for PDMS specimen.

3 Results

3.1 Displacement Errors of Rigid Body Translation

Displacement errors are calculated using Equation 1, where u and v are the in-plane, horizontal and vertical displacements within the image, respectively, and is compared to the actuator translation, w_0.

$$\Delta w_{2D} = \left| \sqrt{u^2 + v^2} - w_0 \right|$$
$$\Delta w_{3D} = \left| \sqrt{u^2 + v^2 + w^2} - w_0 \right| \quad (1)$$

3.1.1 2D DIC on metal

In Figure 6, the error for the associated applied displacement is shown with black data points representing the errors for rigid body translation under white light while the blue points represent the errors for the same test with blue light.

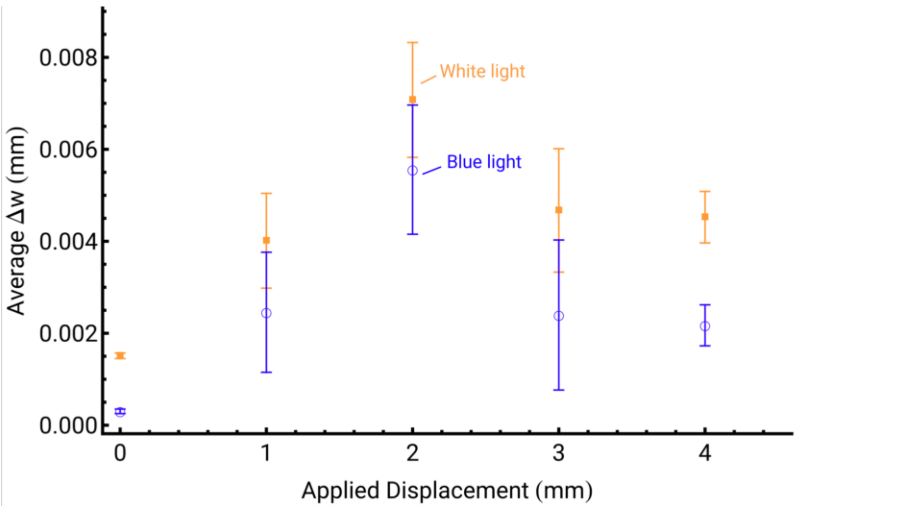

Fig. 6: Results from rigid body translation tests of NiTi.

3.1.2 3D + 2D DIC on silicone rubber

Errors in the applied displacements of Figure 7 varied at the initial stages but were consistently lower with cross-polarized blue light as specimens were translated across the FOV.

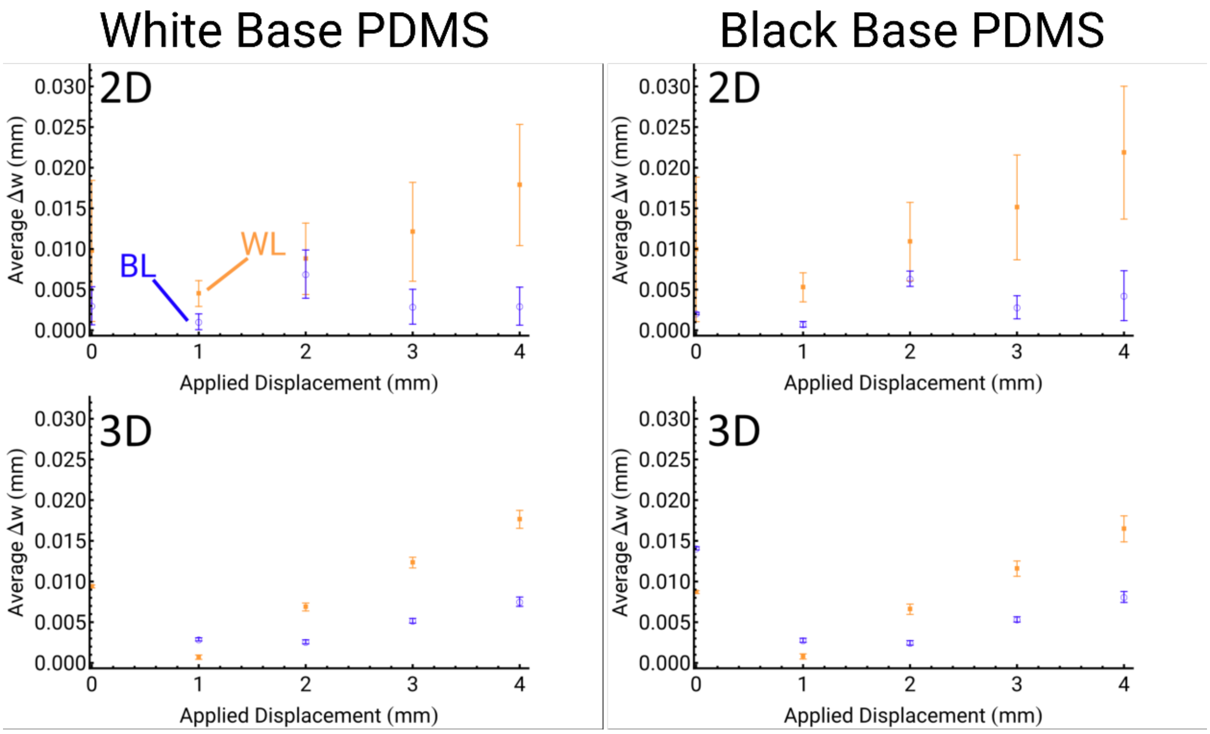

Fig. 7: Results from rigid body translation tests of the silicone rubber material where BL refers to the blue light illumination and WL, the white light illumination.

3.2 Gray Value Count

In the 8-bit sensors, the gray value ranges from 0-255. On the 8-bit sensor dynamic range, values near 0 designate low intensities of light and thus the darkest parts of the image. In contrast, pixels with high intensities of light indicate the brightest parts of the image and are skewed towards grey value counts of 255. Histograms of the gray value count were used to compare image contrast between cross-polarized white and blue light illumination, such as in Figure 8. This was done by using the nominal distribution width, which is defined as the region containing 90% of the grayscale values.

3.2.1 Rigid Body Translation

In the 2D scenarios with telecentric lenses, all histograms from blue light images had an increased nominal distribution width when compared to those from white light. For the NiTi specimen, the histogram width increased by 18 gray value counts, or 14.6% of the 8-bit sensor's dynamic range. The white base PDMS sample saw an increase of 8 counts, or 7%, while the black base PDMS sample had an increase of 41 gray value counts, or 43%.

The histograms taken from 3D DIC resulted in a decrease of 14 gray counts, or -20.5% for the white base PDMS and 6 gray counts, or -8.8% for the black base PDMS. While the spread decreased for the for the 3D DIC cases, the shift towards the lower grey values indicates a darker black point. This is particularly noticeable in the white base specimen in which the histogram is shifted to the left in addition to a peak of values at a grey value of 30.

Rigid body translation tests isolate the imaging or sensor noise from speckle pattern deformation as each speckle translates without changing shape or relative location to other speckles. The improvement in contrast of the images by way of increased black point and bimodal distributions in the histograms of Figure 8 is consistent with the reduced displacement errors.

3.2.2 Uniaxial Tension: 2D DIC on Metals

The grayscale histograms were consistent across the three strain levels for each metal specimen as seen in Figure 9. The width of the histograms decreased by 10 gray value counts, or 6%, for both specimens at all strain levels. Under blue light, gray value distributions are all bimodal for the acrylic surface of the metal specimen.

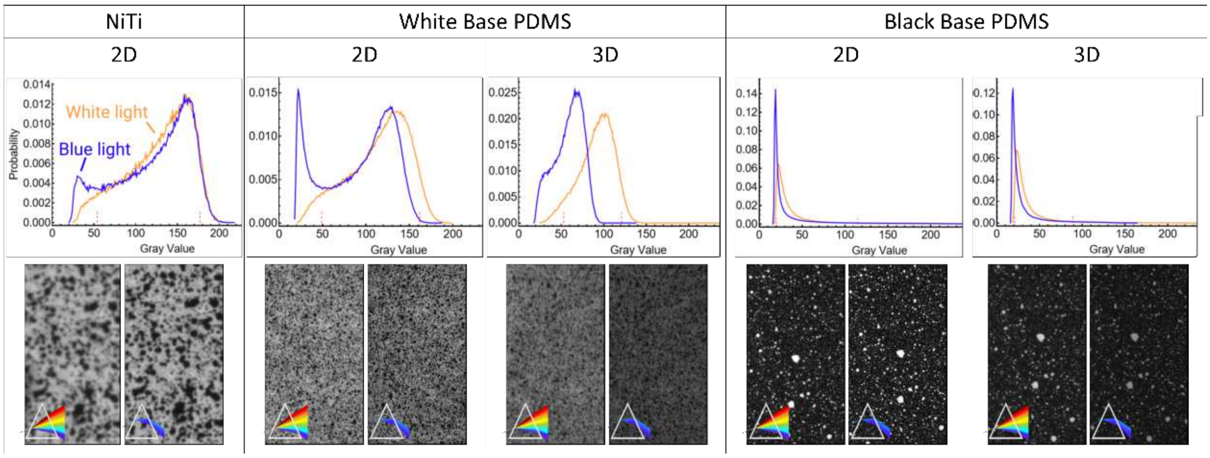

Fig. 8: Histograms of rigid body translation tests.

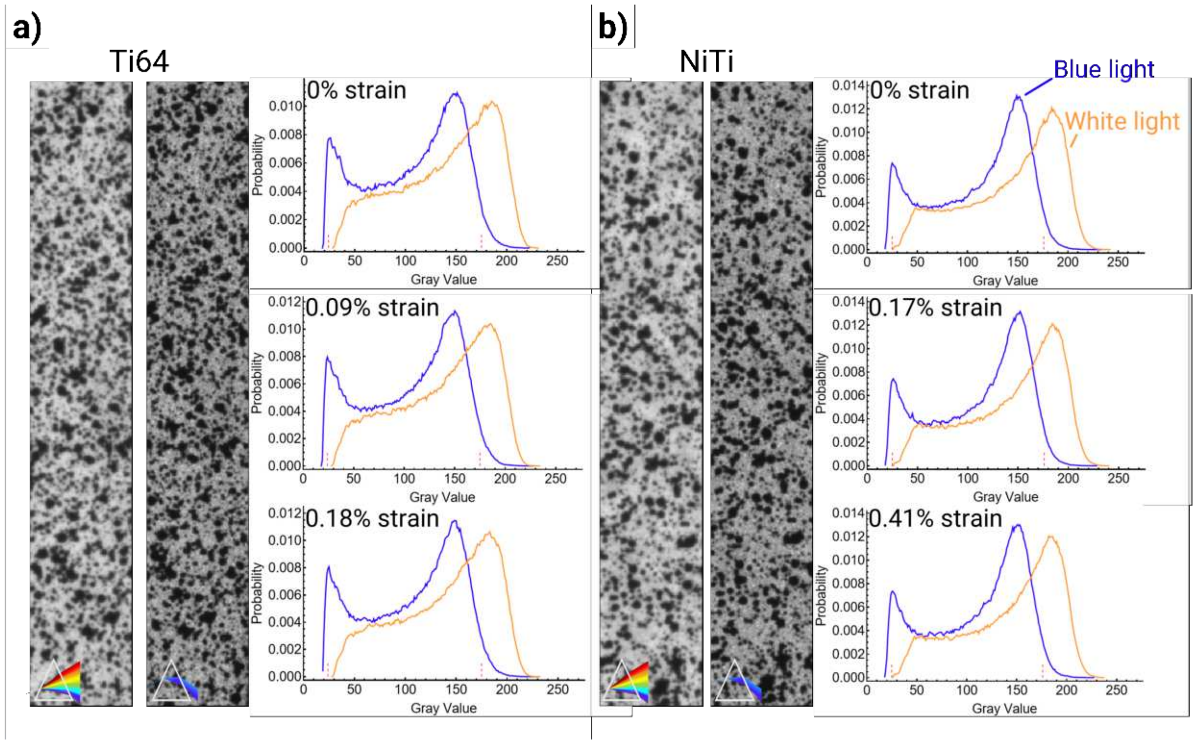

Fig. 9: Gray value count histograms for Ti64 and NiTi specimen with representative images for comparison.

3.2.3 Uniaxial Tension: 3D DIC on PDMS

For silicone rubber, Figure 10a and 10b show the two color schemes for silicone rubber specimen. The histograms in Figure 10, show a general shift to toward lower gray values for the blue light tests. At the reference images or 0% strain, the blue light increased the contrast of the white base material by 8 gray value counts, or 12.9%; the contrast of the black base, 10 gray value counts or 17.5%. At 50% strain, the contrast of the white base material improved by 16 counts or 21.1%; the black base material, 12 counts, or 21.1%.

3.3 Correlation Confidence and Optimal Subset Size

In Correlated Solutions' Vic software suite, the optimal subset size (OSS) is calculated automatically to optimize a confidence match of 0.01 pixel for a default assumed camera noise level of 8. For an image, the user can choose a lower subset size than the suggested OSS at the expense of higher uncertainty

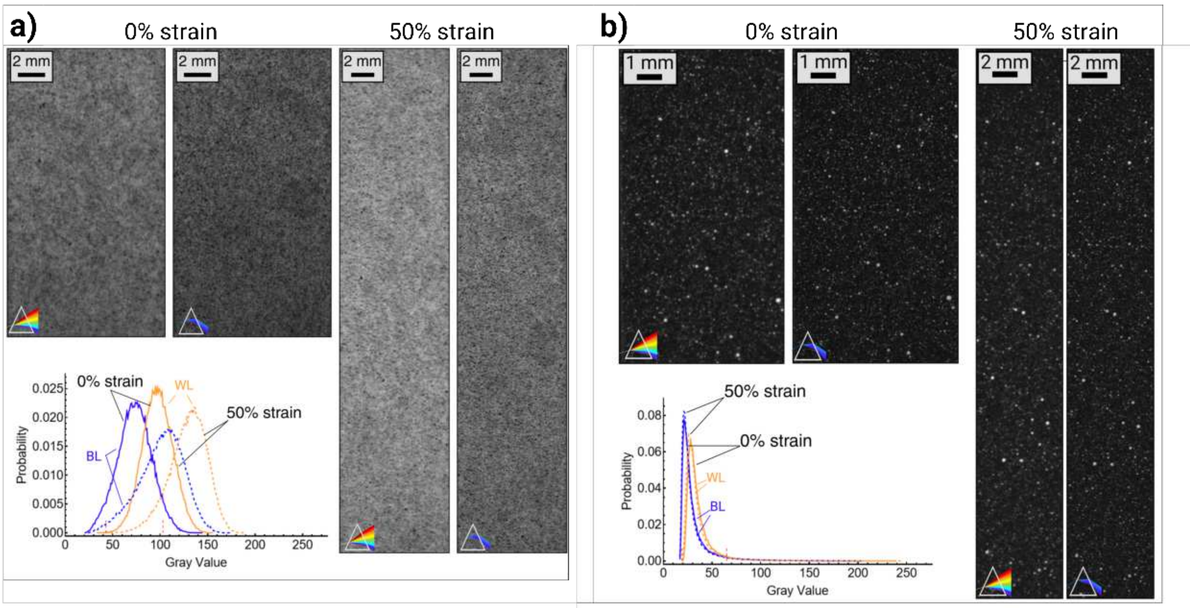

Fig. 10: Gray value count histograms for PDMS specimens at 0% (denoted by a solid line) and 50% strains (denoted by a dashed line).

in the correlation, which can lead to erroneous deformation measurements and dropped areas of data. After running a correlation over test images, each file has an associated correlation confidence interval (CCI) that is one standard deviation in each subset; this can be output directly from the software for each pixel in an image file. The CCI is a measurement of correlation accuracy.

For all tests, the OSS was lower for all tests under blue light illumination by at least 10 subset sizes, summarized in Figure 11f. The CCI for each material and illumination scenario are shown in Figure 11. With a smaller subset size, the strain field is more refined which is particularly important for strains near edges, cracks, or holes.

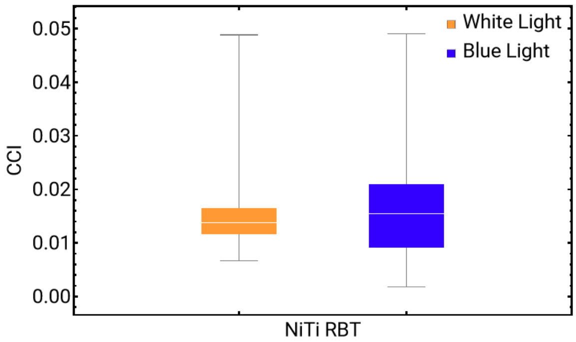

(a) Correlation confidence interval for uniaxial tests of metal specimens with 2D DIC.

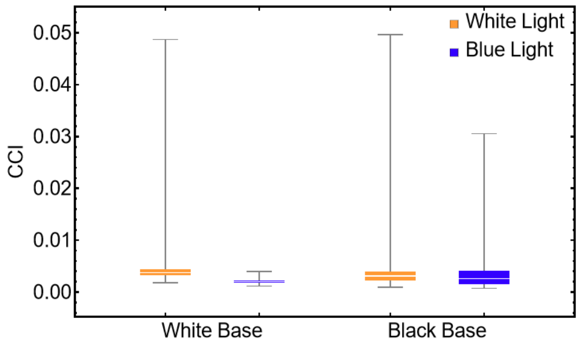

(b) Correlation confidence interval for rigid body displacement tests of Dragon Skin 10 specimens with 2D DIC.

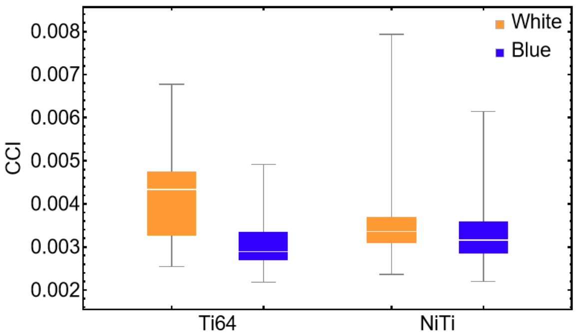

(c) Correlation confidence interval for uniaxial tests of metal specimens with 2D DIC.

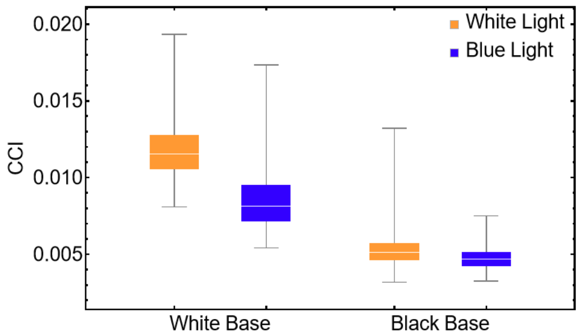

(d) Correlation confidence interval for uniaxial tests of Dragon Skin 10 specimens with 3D DIC.

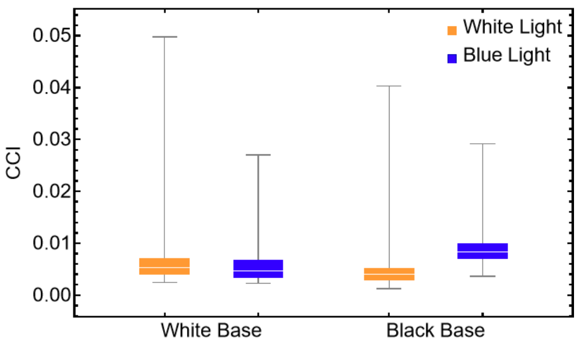

(e) Correlation confidence interval for rigid body displacement tests of Dragon Skin 10 specimens with 3D DIC.

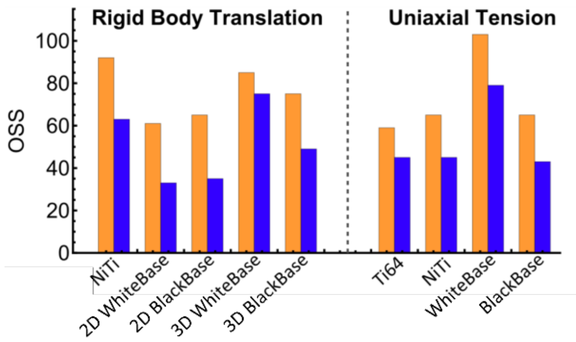

(f) Bar graphs of optimal subset size (OSS) for each sample under different lighting scenarios. The cross polarized blue light decreased optimal subset sizing across all tests.

Fig. 11: Correlation confidence interval (CCI) box-whisker charts for and optimal subset size (OSS) suggestions for all tests.

3.4 Imaging Curved Complex Surfaces for DIC

The key achievement of this work is the successful application to curved, complex surfaces, demonstrated by drastic improvement from sparse correlation under cross-polarized white light to complete surface correlation using cross-polarized blue light. The lattice shown in Figure 12 consists of a 2x2x2 arrangement of cuboctahedron unit cells, fabricated from Dragon Skin 10. A white base layer of silicone rubber was applied, followed by black acrylic speckles produced in the same manner as described in Section 2.1.2, and a clear coat. The lattice was then bathed in mineral oil, producing a reflective surface.

Imaging was performed with two FLIR Grasshopper 3 cameras fitted with 10 mm tube extenders and the filter configurations described in Table 2. Given that the tube extenders darken the image, two additional halogen lights were used in the white light illumination. In an effort to diffuse as much white light as possible, white polyester fabric was placed in front of the light sources. Despite these efforts, the imaged surface suffered from persistent specular reflection, leading to decorrelation. To compensate, correlation thresholds were adjusted: the consistency threshold was raised to 0.03 px and the matchability threshold to 0.14 px. With these adjustments the lattice surface could not be rendered under white light.

Using our method of cross polarized blue light, we achieved full surface correlation across the entire complex curved geometry. Figure 12 summarizes the two illumination approaches: white light proved inadequate for rendering the full lattice surface despite aggressive thresholding adjustments, whereas the blue light allowed the DIC software to capture the complete surface using standard thresholds. The blue light approach eliminates the problematic specular component visible on all lattice members under white light, while the improved scatter of light, absence of optical bloom and chromatic aberration yields improved contrast and clarity which was unattainable using conventional DIC methods.

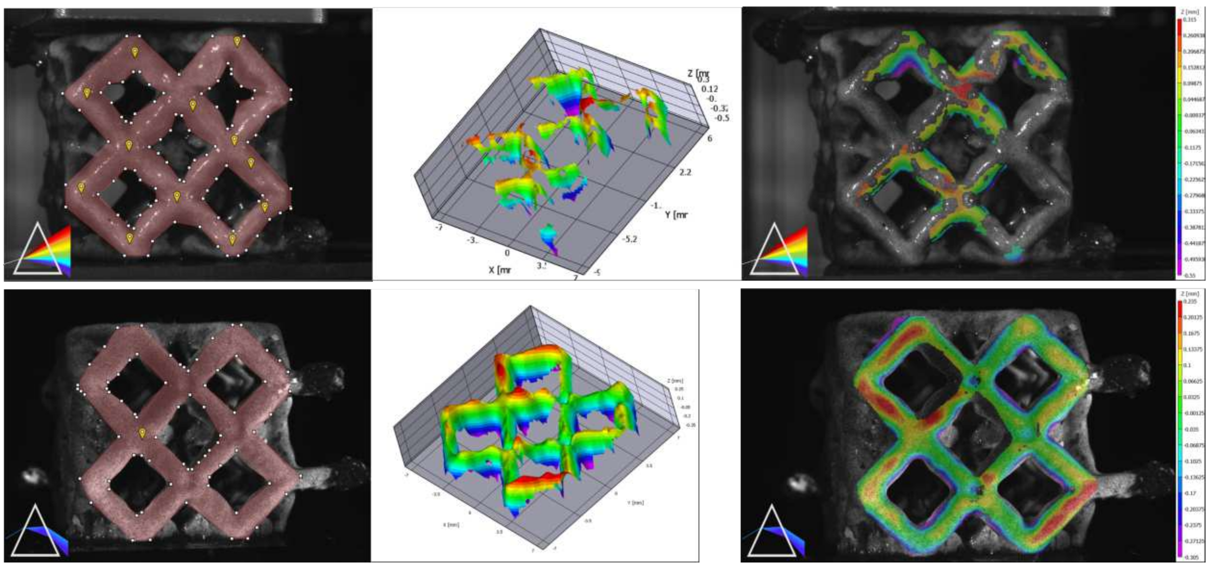

Fig. 12: Comparison of DIC on a oil-bathed silicone rubber lattice under cross polarized white light (top row) and blue light (bottom row).

4 Discussion

While most cases showed improved CCI with blue light and filtering, one outlier dataset deviated from this: the CCI for the black base PDMS sample during rigid body translation was slightly worse than the control, even though the variability was reduced, as indicated by the shorter whisker on the box-plot of 11e. However, this particular dataset had the largest improvement of all datasets in contrast by 43% and also had a 35% decrease for the suggested subset size. A correlation was performed for a select area of the specimen with the typical starting values of tracking every 7th pixel in a subset of 29x29 pixels which is shown in Figure 13. Under cross-polarized white light, the software simply drops data within the speckle but with the cross-polarized blue light, the speckle contains enough variation in gray value of the pixels for the correlation to include points within the speckle itself.

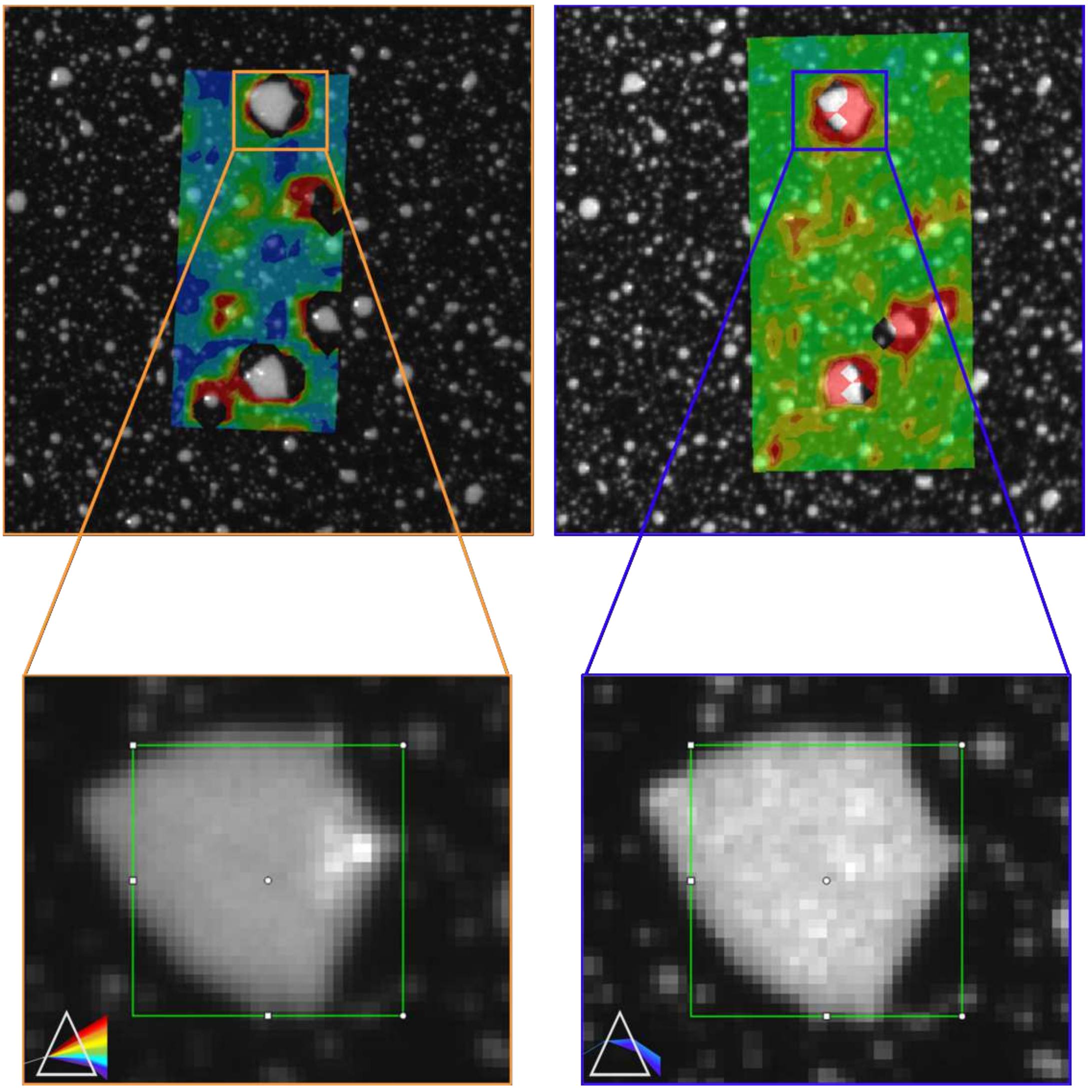

Fig. 13: The rigid body translation test of the black base PDMS sample had improved displacement errors, contrast, and OSS but showed a decrease in CCI. The 29x29 px subset size is shown on the large speckle within the green box in the callout.

The improvements to DIC performance can be attributed to several optical mechanisms. In 1833, mathematician and astronomer Sir George Airy described the optical phenomenon of concentric diffraction rings surrounding a star [26]. He inferred that "[t]he image of a star will not be a point but a bright circle surrounded by a series of bright rings" and that the diameter of these rings will be based solely on the aperture, $(f/\#)$, of the imaging system and the wavelength, λ, of light. This relationship is given by Equation 2. This equation is used for evaluating the minimum spot size—or effective resolution—of a camera and lens system.

$$\varnothing_{\text{Airy Disk}} \approx 2.44\lambda(f/\#) \tag{2}$$

As mentioned, white light contains all visible wavelengths of light, each wavelength producing its own Airy disk. When combined, the superposition of these discs increases image blur. Table 3 compares Airy disk diameters for blue, green, and red light across several apertures. Longer wavelengths are diffracted more and thus have larger minimum spot sizes. Using blue light reduces the minimum spot size; in our 3D uniaxial tension setup, the minimum spot size is roughly 4.6 μm.

In addition to reducing the Airy disk size, blue light illumination minimizes chromatic aberration. Chromatic aberration occurs due to the differences in refraction physics of different wavelengths of light through a solid medium. These shifts can occur along the optical axis or within the focal plane. Longitudinal chromatic aberration occurs when different wavelengths focus at different positions along the optical axis, producing color fringing. Transverse chromatic aberration occurs when wavelengths focus at different positions within the focal plane, altering image magnification. Both types introduce blur and apparent image displacement. In grayscale imaging, eliminating wavelength variation (i.e. *not* using white light) reduces these effects and minimizes variations in pixel intensity at object boundaries [19, 20].

		Aperture (f/#)					
Color	Wavelength [nm]	2	2.8	4	8	11	16
Blue	470	2.29	3.21	4.59	9.17	12.61	36.70
Green	580	2.83	3.96	5.66	11.32	15.57	45.29
Red	650	3.17	4.44	6.34	12.69	17.45	50.75

Table 3: Example Airy disk diameters in microns for blue, green, and red light with different apertures. Increased wavelength increases diameter.

A third contributing factor to DIC improvements is wavelength dependent scattering. Blue illumination experiences stronger Rayleigh scattering than longer wavelengths, and Mie scattering becomes significant when surface or particle features are comparable to the illumination wavelength. Surface imperfections, refractive-index mismatches, and Fresnel reflections further diffuse reflection, taking away the intensity of the specular component. These effects helps suppress glare on complex curved surfaces, where surface normals vary continuously and traditional cross-polarization cannot fully block specular reflections. The AOI images in Section 3.4 make this evident by the clear absence of specular reflection when imaged with our method.

5 Conclusion

Blue light illumination, combined with cross polarization, improves DIC performance. First, by reduction in the Airy disk due to the short wavelength, which improves resolution of the imaging system. Second, by minimizing chromatic aberration, resulting in less image blur. Third, by Rayleigh scattering, which provides better diffuse reflection due to the short wavelength.

The combination of these effects increase contrast, lower optimal subset size suggestions and increase correlation confidence. These benefits extended to our test case: a highly reflective, oil-bathed silicone lattice. The combination of blue light and cross polarization enabled nearly complete surface correlation which will be helpful in applications where surface modification is impossible or undesirable, and where complex geometry introduces severe glare.

By using the standard acrylic speckle patterns, switching to a monochrome light source, adding a bandpass filter, this method can be easily implemented to improve DIC image quality.

Declarations

Acknowledgments. The authors would like to thank the funding sources for the support of this work: NSF EFRI Grant No. 1935312, NSF Grant No. 2340688, SMST Founder's Grant, NSF Grant No. 2320690 No competing financial interests exist.

Author Contributions. CS: Conceptualization, Data curation, Formal Analysis, Investigation, Methodology, Project administration, Validation, Visualization, Writing – original draft, Writing – review & editing; ML: Conceptualization, Data curation, Investigation, Validation, Writing – original draft, Writing – review & editing; WL: Conceptualization, Funding acquisition, Methodology, Resources, Supervision, Writing – review & editing; MK: Conceptualization, Funding acquisition, Methodology, Resources, Supervision, Writing – review & editing

References

[1] Li, W., Zhang, M., Liang, J., Ren, M., Zong, Y., Ye, M., Li, Y.: Accurate and efficient 3d reconstruction system for the human body with color texture based on DIC **127**, 105946 https://doi.org/10.1016/j.optlaseng.2019.105946 . Accessed 2025-07-30

[2] Bigger, R., Blaysat, B., Boo, C., Grewer, M., Hu, J., Jones, A., Klein, M., Lava, P., Pankow, M., Raghavan, K., Reu, P., Schmidt, T., Siebert, T., Simonsen, M., Trim, A., Turner, D., Vieira, A., Weikert, T., Jones, E., Iadicola, M.: A good practices guide for digital image correlation. Technical report, International Digital Image Correlation Society. https://doi.org/10.32720/idics/gpg.ed1/print.format . http://idics.org/guide/ Accessed 2025-07-19

[3] Pan, B.: Digital image correlation for surface deformation measurement: historical developments, recent advances and future goals **29**(8), 082001 https://doi.org/10.1088/1361-6501/aac55b . Publisher: IOP Publishing. Accessed 2025-07-30

[4] Cheng, X., Wang, S., Wei, H., Sun, X., Xin, L., Li, L., Li, C., Wang, Z.: Application of stereo digital image correlation on facial expressions sensing **24**(8), 2450 https://doi.org/10.3390/s24082450 . Accessed 2025-07-19

[5] Ha, N.S., Vang, H.M., Goo, N.S.: Modal analysis using digital image correlation technique: An application to artificial wing mimicking beetle's hind wing **55**(5), 989–998 https://doi.org/10.1007/s11340-015-9987-2 . Accessed 2025-07-19

[6] LePage, W.S., Shaw, J.A., Daly, S.H.: Optimum paint sequence for speckle patterns in digital image correlation **41**(5), 557–563 https://doi.org/10.1007/s40799-017-0192-3 . Publisher: Springer Science and Business Media LLC. Accessed 2025-07-19

[7] LePage, W.S., Daly, S.H., Shaw, J.A.: Cross polarization for improved digital image correlation **56**(6), 969–985 https://doi.org/10.1007/s11340-016-0129-2 . Accessed 2025-07-19

[8] Dong, B., Li, C., Pan, B.: Fluorescent digital image correlation applied for macroscale deformation measurement **117**(4), 044101 https://doi.org/10.1063/5.0016384 . Accessed 2025-07-19

[9] Berke, R.B., Lambros, J.: Ultraviolet digital image correlation (UV-DIC) for high temperature applications **85**(4), 045121 https://doi.org/10.1063/1.4871991 . Accessed 2025-07-30

[10] Yan, T., Su, Y., Zhang, Q.: Precise 3d shape measurement of three-dimensional digital image correlation for complex surfaces **61**(1), 68–73 https://doi.org/10.1007/s11431-017-9125-7 . Accessed 2025-07-31

[11] Zhao, K., Qiu, H., Gao, C., Jiang, L.: Glare suppressed 3d mapping system based on linear polarization filtering and binocular vision fusion **15**(1), 20998 https://doi.org/10.1038/s41598-025-06887-w . Publisher: Nature Publishing Group. Accessed 2025-07-19

[12] Locke, R.C., Peloquin, J.M., Lemmon, E.A., Szostek, A., Elliott, D.M., Killian, M.L.: Strain distribution of intact rat rotator cuff tendon-to-bone attachments and attachments with defects **139**(111007) https://doi.org/10.1115/1.4038111 . Accessed 2025-07-31

[13] Turner, J.A., Menary, G.H., Martin, P.J.: Biaxial characterization of poly(ether-ether-ketone) for thermoforming: A comparison between bulge and in-plane biaxial testing **59**(9), 1853–1865 https://doi.org/10.1002/pen.25185 . _eprint: https://4spepublications.onlinelibrary.wiley.com/doi/pdf/10.1002/pen.25185. Accessed 2025-07-31

[14] Berfield, T.A., Patel, J.K., Shimmin, R.G., Braun, P.V., Lambros, J., Sottos, N.R.: Micro- and nanoscale deformation measurement of surface and internal planes via digital image correlation **47**(1), 51–62 https://doi.org/10.1007/s11340-006-0531-2 . Accessed 2026-03-06

[15] Hu, Z., Luo, H., Du, Y., Lu, H.: Fluorescent stereo microscopy for 3d surface profilometry and

deformation mapping **21**(10), 11808–11818 https://doi.org/10.1364/OE.21.011808 . Accessed 2025-07-31

[16] Mz, I., A, N., Sc, P.: Photobleaching and its kinetics of fluorescein dyes in PVA polymer matrices: A review. Accessed 2025-07-31

[17] Frey, J., Christenson, C., Singer, K.: Photobleaching of fluorescent dyes in polymer films

[18] Dibbern-Brunelli, D., Oliveira, M.G., Atvars, T.D.Z.: Temperature dependence of the photobleaching process of fluorescein in poly(vinyl alcohol) **85**(3), 285–289 https://doi.org/10.1016/1010-6030(94)03915-H . Accessed 2025-07-31

[19] 1stVision: Monochrome light better for machine vision than white light. https://www.1stvision.com/machine-vision-solutions/2024/05/monochrome-light-better-for-machine-vision-than-white-light.html Accessed 2025-07-31

[20] Chromatic Aberration. http://hyperphysics.phy-astr.gsu.edu/hbase/geoopt/aber2.html Accessed 2025-08-10

[21] Chen, X., Xu, N., Yang, L., Xiang, D.: High temperature displacement and strain measurement using a monochromatic light illuminated stereo digital image correlation system **23**(12), 125603 https://doi.org/10.1088/0957-0233/23/12/125603 . Accessed 2025-08-11

[22] Pan, B., Wu, D., Yu, L.: Optimization of a three-dimensional digital image correlation system for deformation measurements in extreme environments **51**(19), 4409–4419 https://doi.org/10.1364/AO.51.004409 . Publisher: Optica Publishing Group. Accessed 2025-08-17

[23] Dragon Skin™ 10 MEDIUM Product Information. https://www.smooth-on.com/products/dragon-skin-10-medium/ Accessed 2025-08-10

[24] Hillborg, H., Sandelin, M., Gedde, U.W.: Hydrophobic recovery of polydimethylsiloxane after exposure to partial discharges as a function of crosslink density **42**(17), 7349–7362 https://doi.org/10.1016/S0032-3861(01)00202-6 . Accessed 2025-08-10

[25] Martinez, M.A., Abenojar, J., Armentia, S.: Environmentally friendly plasma activation of acrylonitrile–butadiene–styrene and polydimethylsiloxane surfaces to improve paint adhesion **8**(12), 428 https://doi.org/10.3390/coatings8120428 . Publisher: Multidisciplinary Digital Publishing Institute. Accessed 2025-08-10

[26] Cambridge Philosophical Society: Transactions of the Cambridge Philosophical Society. http://archive.org/details/transactionsofca05camb Accessed 2025-08-10